PHYSICAL REVIEW B **70**, 024421 (2004)

NMR and dc susceptibility studies of $NaVGe_2O_6$

B. Pedrini,[1] J. L. Gavilano,[1] D. Rau,[1] H. R. Ott,[1] S. M. Kazakov,[1] J. Karpinski,[1] and S. Wessel[2]
[1]*Laboratorium für Festkörperphysik, ETH-Hönggerberg, CH-8093 Zürich, Switzerland*
[2]*Institut für Theoretische Physik, ETH-Hönggerberg, CH-8093 Zürich, Switzerland*

(Received 17 February 2004; published 29 July 2004)

We report the results of measurements of the dc magnetic susceptibility χ and of the ^{23}Na nuclear magnetic resonance (NMR) response of $NaVGe_2O_6$, a material in which the V ions form a network of interacting one-dimensional spin $S=1$ chains. The experiments were made at temperatures between 2.5 and 300 K. The $\chi(T)$ data suggest that the formation of the expected low-temperature Haldane phase is intercepted by an antiferromagnetic phase transition at $T_N=18$ K. The transition is also reflected in the ^{23}Na NMR spectra and the corresponding spin-lattice relaxation rate $T_1^{-1}(T)$. In the ordered phase, $T_1^{-1}(T)$ decreases by orders of magnitude with decreasing temperature, indicating the formation of a gap of the order of 12 K in the magnetic excitation spectrum.

DOI: 10.1103/PhysRevB.70.024421 PACS number(s): 75.10.Pq, 75.50.Ee, 76.60.−k

I. INTRODUCTION

Quasi-one-dimensional (1D) spin systems have recently been the subject of both theoretical and experimental investigations. It was shown theoretically[1] that for chains of antiferromagnetically coupled integer spins the ground state is separated by an energy gap Δ_H from the magnetic excitations. This was later confirmed experimentally for many systems,[2] including the inorganic compounds $AgVP_2O_6$,[3] $CsNiCl_3$,[4] $YBaNiO_5$,[5] as well as for organic substances.[6]

In 1999, a new member, $LiVGe_2O_6$, was added to the list of quasi-1D magnets.[7] From the temperature dependence of the magnetic susceptibility, the expected spin gap Δ_H/k_B was estimated to be about 19 K. Instead of developing the Haldane phase at low temperatures, however, the compound exhibits a transition to a three-dimensional (3D) magnetically ordered state at 25 K. This was established by NMR,[8,9] as well as by neutron-diffraction experiments.[10]

Since many aspects of the magnetically ordered state of $LiVGe_2O_6$ remain a mystery, and the V−V interaction depends on details of the V−O−V bonds, we consider it as worthwile to carefully investigate the magnetic properties of other materials related to $LiVGe_2O_6$. In this work, we report a study of the related compound $NaVGe_2O_6$. Although $LiVGe_2O_6$ and $NaVGe_2O_6$ exhibit many similar features, they are not identical at all. In particular, the differences in the ionic radii of Li and Na seem to be reflected in subtle structural changes. Our dc susceptibility measurements indicate a magnetic phase transition at 18 K. We provide a detailed analysis of the magnetic susceptibility of $NaVGe_2O_6$ (and also of $LiVGe_2O_6$), including computer-based model calculations. This leads to estimates of the intra- and interchain coupling parameters, indicating that for $NaVGe_2O_6$, the intrachain coupling is weaker and the 1D character less pronounced. From the estimated values we conclude that the non-negligible interchain coupling is the main cause for the absence of the expected formation of the Haldane state at low temperatures. The results of subsequent ^{23}Na NMR experiments, including the mapping of NMR spectra and measurements of both the spin-lattice and spin-spin relaxation rates, confirm the existence of a phase transition, most likely to a 3D antiferromagnetically ordered state.

The paper is organized as follows. In Sec. II we provide information on the sample. In Sec. III we report on the dc susceptibility measurements, and in Secs. IV–VI we describe and discuss the results of the NMR experiments. In Sec. VII we compare the magnetic properties of the related compounds $NaVGe_2O_6$ and $LiVGe_2O_6$.

II. CRYSTAL STRUCTURE AND SAMPLE

$NaVGe_2O_6$ crystallizes with a monoclinic structure, space group $P2_1/c$. The $NaVGe_2O_6$ powder sample was prepared following the procedure described in Ref. 11. A stoichiometric mixture of GeO_2 (Aldrich, 99.998%), V_2O_3 (Aldrich, 99.99%), and $Na_2Ge_2O_5$ was pressed into pellets and annealed at 900 °C for 70 h in an evacuated silica tube. $Na_2Ge_2O_5$ was synthesized by heating a mixture of Na_2CO_3 (Aldrich, 99.995%) and GeO_2 at 760 °C for 15 h in air. According to x-ray powder diffraction data, the sample was of single phase with the pyroxene structure. The corresponding lattice parameters are $a=9.9600(5)$, $b=8.8444(4)$, $c=5.4858(2)$ Å, and $\beta=106.50(2)°$. The crystal structure is shown schematically in Fig. 1. It consists of chains of isolated, slightly distorted VO_6 octahedra joined at the edges. These chains are linked but also kept apart by double chains of distorted GeO_4 tetrahedra.

Taking into account the most likely oxidation states of O^{2-}, Na^{1+}, and Ge^{4+}, the V ions are expected to be trivalent. The magnetic moments are thus due to the two 3d electrons localized at the V^{3+} ions, which form an $S=1$ system. Assuming that the interaction beween these moments is due to exchange interaction mediated by the 2p-electrons of the O ions, the intrachain coupling J is anticipated to be much larger than the interchain coupling $J_\perp$ because the former involves only one O site, whereas the latter is spread over two of them.

For our measurements we used a powdered sample, with randomly oriented grains and a mass of 127 mg, correspond-

0163-1829/2004/70(2)/024421(10)/$22.50

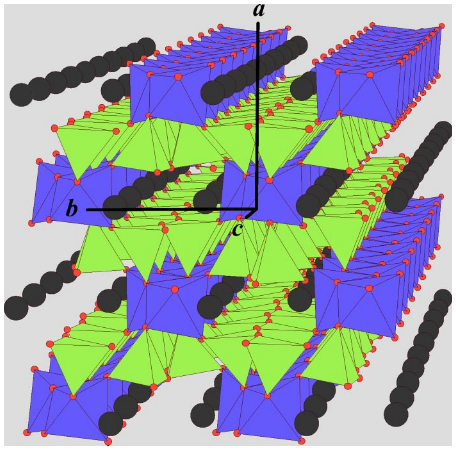

FIG. 1. Schematic representation of the crystal structure of $NaVGe_2O_6$. The crystalline axes are labeled. The V^{3+} ions are located in the centers of the dark-gray VO_6 octahedra, while the Ge^{4+} ions occupy the centers of the light-gray GeO_4 tetrahedra. The Na^+ ions are represented by dark spheres.

ing to 4.04×10^{-4} mol. The diameters of the powder grains were less than 0.1 mm.

III. MAGNETIC SUSCEPTIBILITY

In order to confirm the above-mentioned expected oxidation state of the V ions, we measured the dc magnetic susceptibility $\chi(T)$ between 4 and 340 K, in various fixed magnetic fields between 0.01 and 2 T, using a commercial superconducting quantum interference device magnetometer. For temperatures above 100 K, the data can reasonably be fitted by a Curie-Weiss type of law, i.e., $\chi(T)=\chi_0+C(T-\Theta)^{-1}$. The constant term χ_0 is attributed to magnetic background. In Fig. 2 we display an example of $\chi(T)$, measured in a magnetic field of $H=2$ T. In this field, $\chi_0=1.7\times10^{-3}$ emu/mol. The paramagnetic Curie temperature is $\Theta=-39\pm5$ K, which signals the tendency of the V moments to couple antiferromagnetically. The value of C is

$$C = 0.89 \pm 0.04 \text{ emu mol}^{-1}\text{ K}, \tag{1}$$

where the indicated error range takes into account the values found for other magnetic fields. The effective magnetic moment (in units of μ_B) is thus

$$\mu_{\text{eff}} = \sqrt{\frac{3k_B}{N\mu_B^2}C} = 2.67 \pm 0.05 \tag{2}$$

per V ion. This value is close to the one expected for the V^{3+} (and not V^{4+}) configuration, with quenched orbital moments of the two $3d$ electrons.[12]

The maximum of $\chi(T)$ is reached at the temperature $T_{\max}=25$ K. Below this temperature, a kink in $\chi(T)$ is observed at $T_N=18$ K, as demonstrated in the inset of Fig. 3. The anomaly is much more evident by plotting $d\chi/dT(T)$. The transition temperature T_N is only little, if at all, affected by the value of the magnetic field up to 5 T.

As already anticipated in Sec. II, the chemical composition and the crystal structure of $NaVGe_2O_6$ suggest that the V-moments form a quasi-1D $S=1$ spin system. Nevertheless, the temperature dependence of the susceptibility does not follow the expectations for a collection of independent $S=1$ spin chains. This is evident if one compares the experimental data with the results of quantum Monte Carlo simulations,[13] as shown in Fig. 4. The simulation was performed for a single chain considering the Hamiltonian

$$H = J\sum_i \vec{S}_i \cdot \vec{S}_{i+1}, \tag{3}$$

where $\vec{S}_i$ denotes a spin-1 operator at the ith site, and J is the intrachain coupling. J was adjusted such that the maximum in $\chi(T)$ occurs at 25 K, as is experimentally observed. At high temperatures the experimental and calculated data coin-

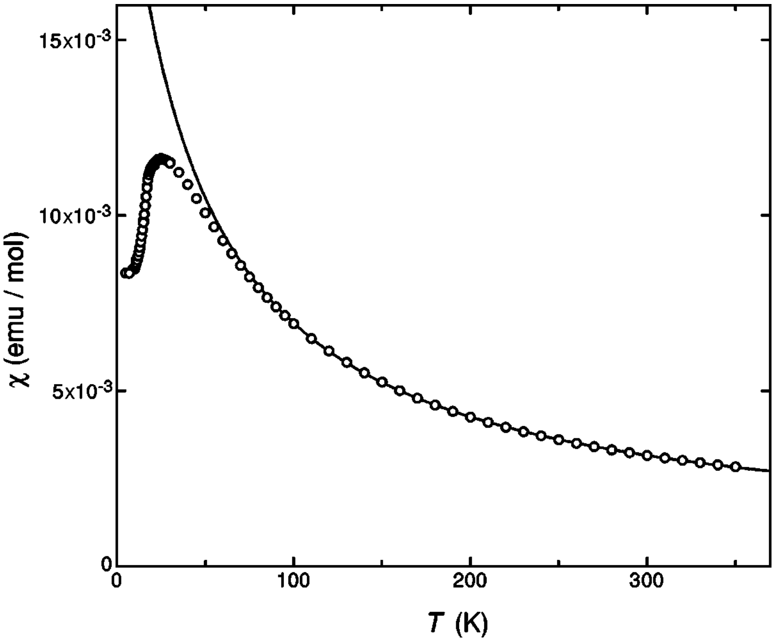

FIG. 2. Magnetic susceptibility χ as a function of temperature T, measured in a magnetic field of $H=2$ T. The solid line represents the best fit to the data for temperatures above 100 K, assuming $\chi(T)=\chi_0+C(T-\Theta)^{-1}$.

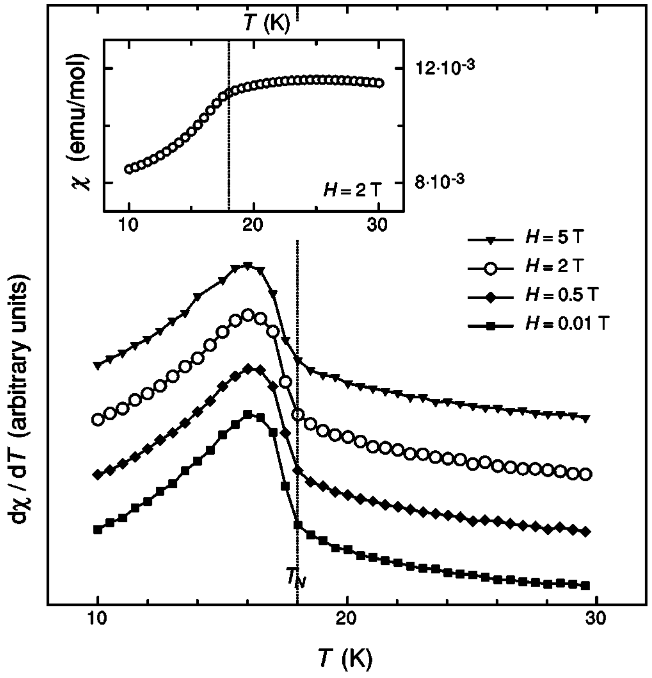

FIG. 3. $d\chi/dT$ as a function of the temperature T for different applied fields. The inset shows $\chi(T)$ at $H=2$ T. The dotted line indicates the low-field transition temperature $T_N=18$ K.

cide. Near 25 K, however, the experimental susceptibility turns out to be smaller than expected for the isolated $S=1$ chains (see Fig. 4), suggesting the existence of some non-negligible interchain coupling. The simulated and experimental $\chi(T)$ data also differ significantly at low temperatures. In particular, the continuous decrease to zero of the calculated $\chi(T)$, revealing the influence of the Haldane gap, is not observed experimentally. Instead a kink in $\chi(T)$ at 18 K indicates a magnetic phase transition.

As is well known from series expansions,[16] even a very small interchain coupling $J_\perp(J_\perp/J>0.026)$ leads to the quenching of the Haldane gap and induces three-dimensonal antiferromagnetic order (see also Ref. 17). As indicated by $\chi(T)$, this indeed seems to occur in $NaVGe_2O_6$, suggesting a non-negligible interchain coupling $J_\perp$ in this compound.

From the measured values of $T_{\max}$ and T_N we can estimate the magnitudes of both the intra- and interchain coupling, and thus their ratio, as follows: Assuming that $T_{\max}$ is unaffected by a small interchain coupling, quantum Monte Carlo simulations of an isolated chain provide a relation between J and $T_{\max}$ of the form

$$\frac{J}{k_B\, T_{\max}} = \frac{1}{1.32} \pm 0.02. \tag{4}$$

The value of the interchain coupling can be estimated from the transition temperature T_N, using a random-phase approximation (RPA). The relevant equation is

$$J_\perp/J = \frac{1}{z\chi^s[k_B T_N/J]}, \tag{5}$$

where χ^s denotes the staggered spin susceptibility of an isolated $S=1$ spin chain. Within conventional RPA[18] $z=4$ equals the number of nearest neighbor chains. Recently, it was found that for both the $S=1/2$ case and the classical Heisenberg model (corresponding to $S\rightarrow\infty$), an improved estimate of $J_\perp/J$ results by using a renormalized value of

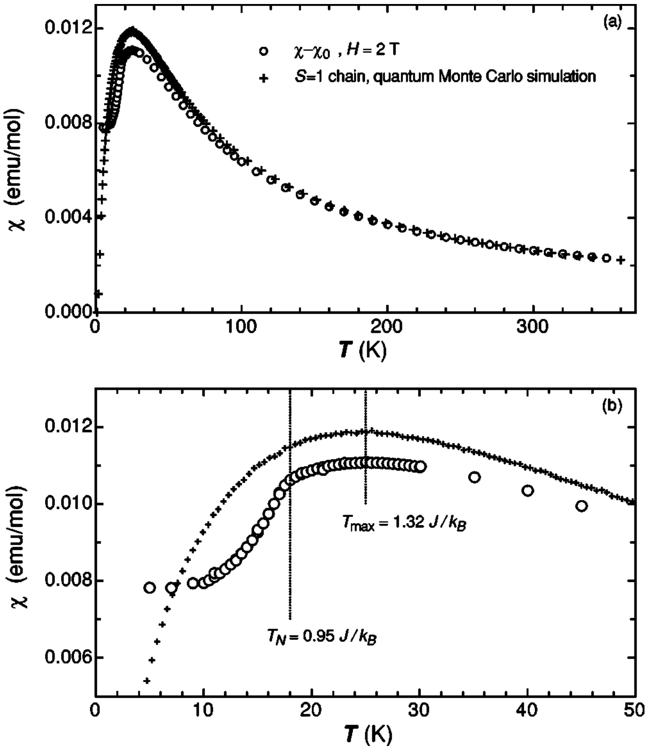

FIG. 4. (a) Experimentally measured $\chi(T)-\chi_0$ as a function of temperature in $H=2$ T, and $\chi(T)$ resulting from quantum Monte Carlo calculations for an $S=1$ spin chain. Panel (b) emphasizes the range $T<50$ K.

$$z = 2.78 \tag{6}$$

for $J_\perp/J<0.2$.[19] We applied this modified RPA also to the $S=1$ case. The result for $(J_\perp/J)$ versus $[k_BT_N/J]$ is shown in Fig. 5, along with an inset for the staggered susceptibility $\chi^s[k_BT/J]$ of an $S=1$ spin chain, as obtained from quantum Monte Carlo calculations. The limit $[k_BT_N/J]\rightarrow 0$ determines the critical value $J_\perp/J=0.02$, i.e., the interchain coupling necessary to suppress the Haldane gap, which is in reasonable agreement with the value estimated in Ref. 16. For $J_\perp/J=0.1$ we find $k_BT_N/J=0.65\pm0.02$ (see dotted lines in Fig. 5), a value which is in good agreement with the result $k_BT_N/J=0.65\pm0.01$ of an explicit quantum Monte Carlo calculation for interacting chains.

The dashed lines in Fig. 5 represent the parameters $J_\perp/J$ and k_BT/J for $NaVGe_2O_6$. Using Eqs. (4) and (5) for $T_{\max}=25\pm0.5$ K and $T_N=18\pm0.5$ K, we obtain for $NaVGe_2O_6$

$$J/k_B = 18.9 \pm 0.5 \text{ K} \tag{7}$$

and

$$J_\perp/J = 0.18 \pm 0.01, \tag{8}$$

i.e.,

$$J_\perp/k_B = 3.4 \pm 0.2 \text{ K}. \tag{9}$$

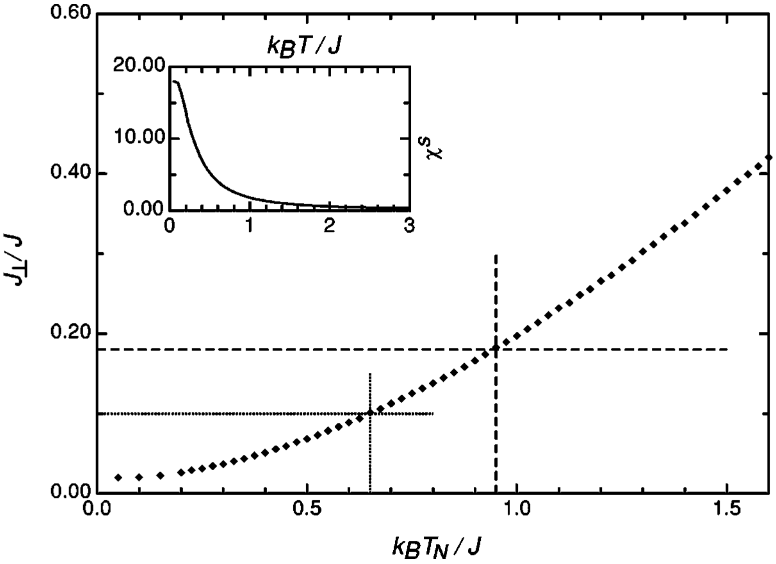

FIG. 5. Interchain coupling as a function of the critical temperature, according to Eq. (5). The extrapolation to $k_BT_N/J=0$ gives $J_\perp/J=0.02$. The parameters $J_\perp/J$ and k_BT_N/J for $NaVGe_2O_6$ are indicated by the dashed lines, while the dotted lines represent $J_\perp/J=0.1$ and the corresponding k_BT_N/J. The inset shows the staggered spin susceptibility χ^s of a $S=1$ spin chain as a function of temperature, as calculated by quantum Monte Carlo simulations.

IV. NMR SPECTRA

With our NMR experiments we probed the ^{23}Na nuclei with a nuclear spin $I=\frac{3}{2}$, a gyromagnetic factor of $\gamma=7.0746\times10^7\ \mathrm{s}^{-1}\ \mathrm{T}^{-1}$, and a quadrupolar moment $|e|Q=0.108|e|\times10^{-24}\ \mathrm{cm}^2$, where e is the electron charge.

^{23}Na NMR spectra were obtained by monitoring the integrated spin-echo intensity as a function of the irradiation frequency, in a fixed magnetic field H or, alternatively, as a function of the magnetic field, at a fixed irradiation frequency. The spin echo was generated with a two-pulse $\pi/2$-delay-π spin-echo sequence, irradiating a frequency window of about 20 kHz.

In Fig. 6, we show examples of the central line of the spectra, corresponding to the $\frac{1}{2}\leftrightarrow-\frac{1}{2}$ transition, measured at three different temperatures above T_N, in a fixed magnetic field of $H=7.0495$ T. The background echo intensity, due to quadrupolar wings, i.e., the transitions $\pm\frac{3}{2}\leftrightarrow\pm\frac{1}{2}$, is subtracted.

The paramagnetic character of the high-temperature phase is reflected in Figs. 7 and 8. In Fig. 7 we plot the relative shift with respect to the unshifted frequency f_0,

$$K_{\mathrm{peak}}=\frac{f_{\mathrm{peak}}-f_0}{f_0}, \tag{10}$$

of the frequency f_{peak} with maximum echo intensity at different temperatures, as a function of the Curie-Weiss part of the dc magnetic susceptibility $\chi(T)$, measured at the corresponding temperatures and in a magnetic field of $H=2$ T. The data for the two different fields collapse onto the same curve. Above $T_{\max}$, $K(\chi)$ can reasonably well be fitted with a linear function, indicating that the temperature dependence of the shift of the NMR line at maximum intensity is of purely magnetic origin. In Fig. 7 we display the best fit to the data at $H=7.0495$ T and for $T>60$ K with the function

$$K_{\mathrm{peak}}=a_{\mathrm{peak}}\chi+c_{\mathrm{peak}}. \tag{11}$$

Within experimental uncertainty, $c_{\mathrm{peak}}\approx0$. The hyperfine coupling corresponding to the peak signal is[20,21]

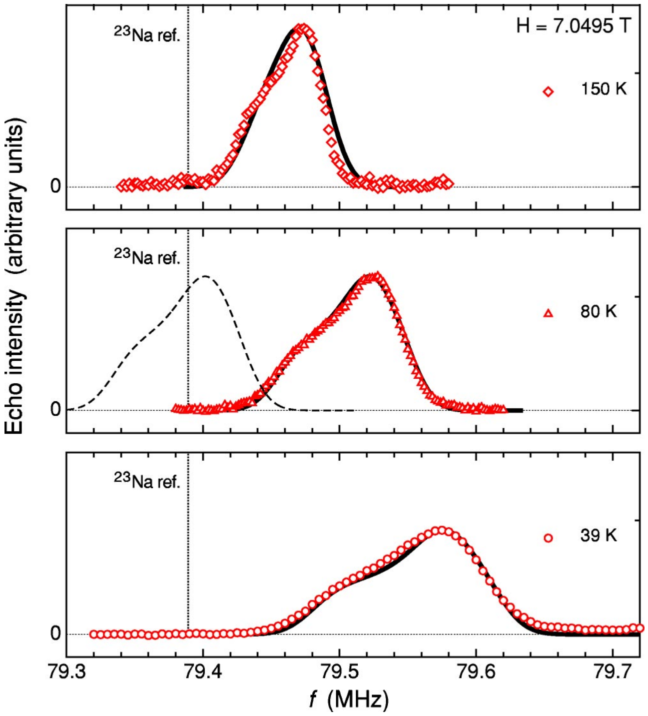

FIG. 6. ^{23}Na NMR spectra of the central line in the paramagnetic phase at three different temperatures in $H=7.0495$ T. The integrated echo intensity (multiplied by the temperature T) is represented as a function of the frequency f. The solid lines represent the intensity $I(f)$, obtained using Eq. (20) and setting $A_0=1140$ G. The dashed curve (shown only for $T=80$ K) corresponds to the calculation with $A_0=0$ G. The dotted line marks the reference position of the ^{23}Na line (79.389 MHz).

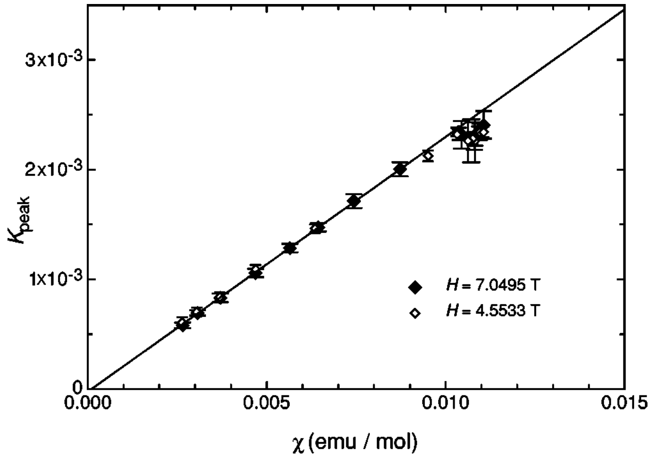

FIG. 7. Relative frequency shift K_{peak} of the maximal intensity NMR line as a function of the dc susceptibility χ, for temperatures above T_N. The solid line is the best linear fit to the data at $H=7.0495$ T, above 60 K.

$$A_{peak} = a_{peak} \cdot N\mu_B = 1300 \pm 50 \text{ G}. \tag{12}$$

In Fig. 8 we plot

$$\sigma_K = \frac{\text{FWHM}}{f_0}, \tag{13}$$

where FWHM is the linewidth and f_0 is the unshifted frequency, at different temperatures, as a function of the Curie-Weiss part of the dc magnetic susceptibility $\chi(T)$, which was measured at the corresponding temperatures and in a magnetic field of $H=2$ T. For $T > T_{max}$ a linear relation $\sigma_K(\chi)$, i.e.,

$$\sigma_K = a_\sigma \chi + c_\sigma, \tag{14}$$

is observed. In Fig. 8, the solid line represents the best fit to the data for $H=7.0495$ T and for $T>60$ K. The corresponding anisotropic hyperfine coupling is[21]

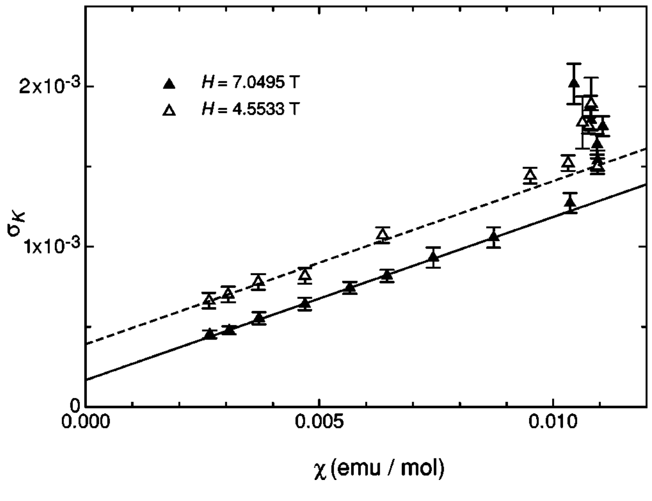

FIG. 8. FWHM of the echo intensity of the central line, divided by the ^{23}Na reference frequency f_0, as a function of the dc susceptibility χ, for temperatures above T_N. The solid and the dashed lines are the best linear fit to the data at $H=7.0495$ and 4.5533 T, respectively, for temperatures above 60 K.

$$\sigma_A = a_\sigma \cdot N\mu_B = 560 \pm 50 \text{ G}. \tag{15}$$

From the value of c_σ for $H=7.0495$ T we find a frequency broadening $\Delta f = c_\sigma f_0 = 14\pm2$ kHz, which is attributed to the nonvanishing irradiation width that indeed is of the same order of magnitude. The dashed line is the best fit to the data for $H=4.5533$ T, keeping a_σ fixed, resulting in $\Delta f = c_\sigma f_0 = 18\pm2$ kHz, again of the same order of magnitude.

The linear relation between σ_K and χ breaks down for $T \leqslant T_{max}$, indicating that below that temperature a substantial degree of antiferromagnetic correlations interferes.

To complete the analysis of the features of the central line in the paramagnetic phase, we compared the experimentally determined line shape with the results of simulations. They were performed by first calculating the lineshape $P^{dip}(A)$ expected for a purely dipolar coupling between the V moments and the Na nuclei, i.e., according to the formula

$$P^{dip}(A) = \int_0^{2\pi} d\phi \int_0^{\pi} d\theta \sin\theta\, \delta[A - A^{dip}(\theta,\phi)]. \tag{16}$$

Here θ and ϕ are the spherical angles describing the orientation of the V moments of 1 μ_B with respect to the cristalline c axis, $A^{dip}(\theta,\phi)$ is the component of the induced hyperfine field at a Na site parallel to the V moments and δ is the delta function. Equation (16) implicitly assumes that (a) the powder sample consists of randomly oriented grains; and (b) the V moments align along the applied external magnetic field.

The integral in Eq. (16) was calculated by approximating it with the sum over a 200×200-points-lattice $\mathcal{G} \subset [0,\pi] \times [0,2\pi]$,

$$P^{dip}(A) \sim \sum_{(\theta,\phi)\in G} \sin\theta\, \Gamma_{\Delta A}[A - A^{dip}(\theta,\phi)], \tag{17}$$

where $\Gamma_{\Delta A}$ is a Gaussian function of width chosen as $\Delta A \approx 20$ G. The resulting line shape $P^{dip}(A)$ is represented as a function of the hyperfine coupling A in Fig. 9. The peak value is reached at

$$A_{peak}^{dip} = 125 \pm 10 \text{ G}, \tag{18}$$

while the mean square deviation is

$$\sigma_A^{dip} = 520 \text{ G}. \tag{19}$$

While σ_A^{dip} is in good agreement with the experimental value σ_A, A_{peak}^{dip} is a factor of 10 smaller than A_{peak} [see Eq. (12)], indicating an additional, relevant nondipolar isotropic hyperfine-field coupling.

For a fixed temperature T and the corresponding susceptibility χ, the signal intensity $I(f)$ as a function of the irradiation frequency f was obtained by

$$I(f) = I_{0,T} \cdot \{P^{dip}[A(f) - A_0]\}_{\Delta f}, \tag{20}$$

where A and f are related by

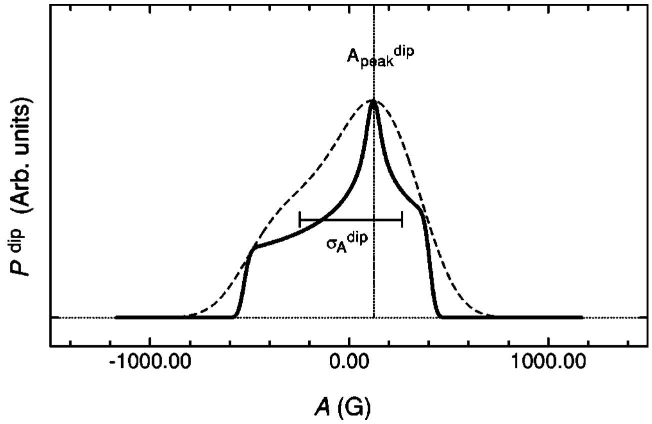

FIG. 9. The solid line represents the shape P^{dip} of the central line calculated assuming dipolar coupling between V moments and Na nuclei, as a function of the hyperfine coupling A. The peak value $A_{\text{peak}}^{\text{dip}}$ and the estimated width σ_A^{dip} are indicated. The dashed line is obtained by broadening the solid line with $\Delta A = 132$ G (corresponding to the same broadening Δf in frequency space as used for $T = 80$ K in Fig. 6).

$$\frac{f - f_0}{f_0} = \frac{A}{N\mu_B}\chi, \tag{21}$$

$I_{0,T}$ is a (temperature dependent) prefactor, and $[\ldots]_{\Delta f}$ indicates the broadening in frequency space with a Gaussian function of width Δf.

In Fig. 6 we plot the calculated line shapes with $\Delta f = 15 \pm 1$ kHz, $A_0 = 1140$ G, and $I_{0,T}$ such that the experimental intensity at the frequency f_{peak} is matched. The parameter A_0 takes into account the above-mentioned nondipolar coupling, whose value has been adjusted to reproduce the experimental data, i.e.,

$$A_{\text{peak}} \approx A_{\text{peak}}^{\text{dip}} + A_0. \tag{22}$$

The experimental line shape is clearly very well accounted for by the simulations. The deformation range of the central NMR line due to second order quadrupolar effects is given by[21]

$$\Delta f_Q^{(2)} = \frac{\nu_Q}{144 f_c}\left[I(I+1) - \frac{3}{4}\right](\eta^2 + 22\eta + 25), \tag{23}$$

where f_c is the Larmor frequency of the ^{23}Na central line, $\nu_Q = e^2 qQ/2h$ is the quadrupolar frequency of ^{23}Na in the electric field gradient eq, and η is the asymmetry parameter of the electric field gradient [$eq = V_{zz}$ is the largest eigenvalue of the electric field gradient tensor, and $\eta = (V_{xx} - V_{yy})/V_{zz}$]. As we shall see below, $\nu_Q = 1.25$ MHz and $\eta = 0.4$. With $f \sim 79.6$ MHz this results in $\Delta f_Q^{(2)} \sim 14$ kHz. The effect is more evident at high temperatures because it is less masked by magnetic broadening. The small deviations of the order of 10 kHz, observed in particular at 150 K, are attributed to such quadrupolar effects.

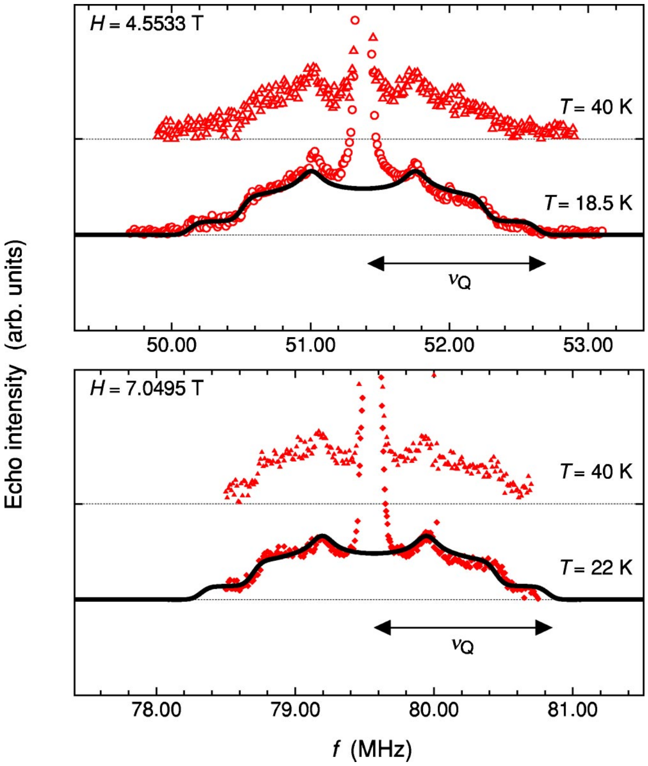

FIG. 10. ^{23}Na NMR spectra around the central line in NaVGe$_2$O$_6$ at two different temperatures above T_N, and in two different fields. The solid lines represent the calculated line shapes due to quadrupolar effects.

As shown in Fig. 10, with decreasing temperatures but still above T_N, we identify features near the central line which are temperature and field independent. They are the signals of the wings due to the transitions $\pm\frac{3}{2} \leftrightarrow \pm\frac{1}{2}$. This claim is supported by the results of comparisons of the measured signals with the signal calculated assuming that the intrinsic part of the central line, at frequency f_c, is unaffected by the orientation of the grains. The shift of the $\pm\frac{3}{2} \leftrightarrow \pm\frac{1}{2}$ transitions is given by[22]

$$\Delta f_Q^{(1)} = \frac{\nu_Q}{2}[3\cos^2\theta - 1 - \eta\sin^2\theta\cos 2\phi]. \tag{24}$$

Here, θ and ϕ are the spherical angles describing the orientation of the principal axes of the electric field gradient tensor with respect to the direction of the applied magnetic field. The solid lines in Fig. 10 represent the calculated signal without the contribution of the central line. The best coincidence is achieved with a quadrupolar frequency of $\nu_Q = 1.25$ MHz and an asymmetry parameter $\eta = 0.4$. The central frequencies f_c were chosen to coincide with the values of the average frequencies of the central line at the corresponding temperature, i.e., to 51.38 MHz (at 4.5533 T) and 79.57 MHz (at 7.0495 T), respectively. The largest eigenvalue of the electric field gradient tensor at the Na-sites is

$$V_{zz} = eq = \frac{2h\nu_Q}{eQ} = 9.58 \times 10^{20}\ \text{V/m}^2. \tag{25}$$

Next, we focus our attention on the ^{23}Na NMR spectra around and below the critical temperature $T_N = 18$ K. In Fig. 11 we show examples of such spectra, measured in the tem-

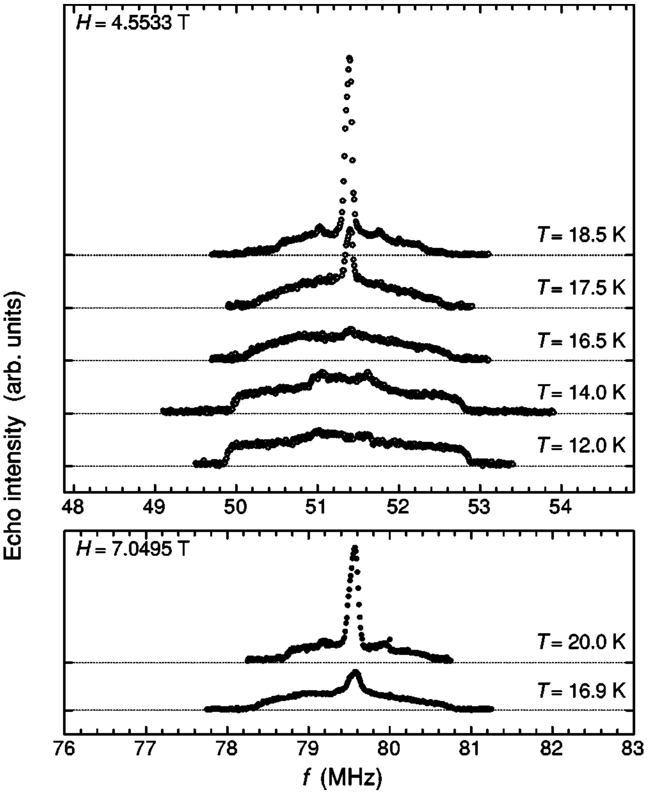

FIG. 11. ^{23}Na NMR spectra of $NaVGe_2O_6$. The echo intensity is represented as a function of the frequency f for selected temperatures below 20 K. The measurements were performed in fixed magnetic fields $H=4.5533$ T (upper panel) and $H=7.0495$ T (lower panel).

perature range between 12 and 20 K, in fixed magnetic fields $H=4.5533$ and 7.0495 T, respectively.

The phase transition at $T_N=18$ K is reflected by a drastic change of the line shape. We note that the central-line intensity decreases rapidly between 18.5 and 16.5 K, indicating that the paramagnetic phase disappears upon crossing the critical temperature from above. At the same time, a much broader signal develops below 18.5 K. At 14.5 K the signal has a well defined, "nearly rectangular" shape, which remains unchanged down to at least 4 K, as evidenced by the signal obtained from a field sweep at a fixed frequency of 80.8 MHz, which is shown in Fig. 12. The observed width and the evolution of the line shape below T_N are both similar at different values of the magnetic field, suggesting that the broadening of the line is due to ordered magnetic moments. This allows one, in particular, to exclude the formation of the Haldane phase below T_N. Indeed, our NMR results cannot be reconciled with the expectations for a nonmagnetic ground state, where a sharp narrowing of the NMR line and a shift towards the reference frequency f_0 should be observed at temperatures $T<\Delta_H/k_B\sim 0.4\ J/k_B=7.6$ K.[23]

The deviation of the observed low-temperature line shape from a rectangle, which is expected for a purely magnetic broadening due to a fixed internal field, in particular the feature in the range between the marks L_1 and R_1 in Fig. 12, is attributed to first order quadrupolar effects. It is not a trivial task to predict the line shape due to the combined effects of an external field, an internal field, and an electric field gradient. The difficulty lies in the uncertainty of the directions of the ordered moments and of the principal axes of the the electric field gradient tensor at the Na sites, respectively. Therefore we discuss this aspect only qualitatively. We assume that at low temperature $(T\ll T_N)$ the signal due to the $\frac{1}{2}\leftrightarrow-\frac{1}{2}$ transition extends from line L_2 to line R_2 in Fig. 12. The intensities in the ranges between L_3 and L_2, as well as between R_2 and R_3, reflect the quadrupolar wings. Their extension, corresponding to about 1 MHz, is compatible with the previously calculated quadrupolar frequency ν_Q. With these assumptions, the magnitude of the internal field, indicated in Fig. 12, is $H_{\text{int}}=1470$ G.

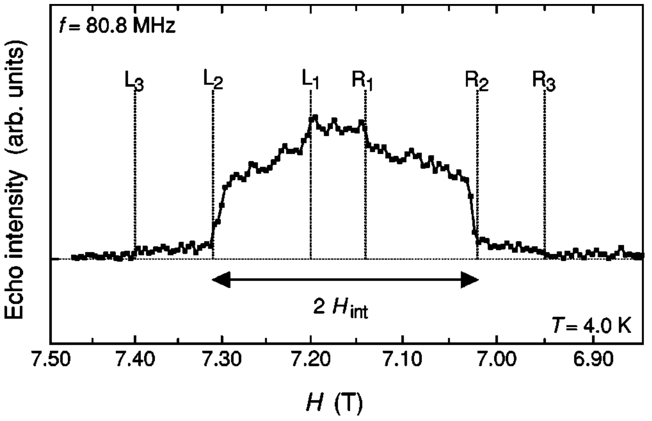

FIG. 12. Example of a ^{23}Na NMR spectrum of $NaVGe_2O_6$ at 4 K. The echo intensity is plotted as a function of the magnetic field H. The measurements were performed at a fixed irradiation frequency of 80.8 MHz.

As a plausibility check for the value of the internal field H_{int} established above, we computed the dipolar field at the Na sites due to three-dimensionally ordered magnetic moments at the V sites. The g-factor for the V^{3+} ions is given by the effective moment found in Eq. (2) as $g=\mu_{\text{eff}}/\sqrt{S(S+1)}=1.89$. In Table I we show the values of the calculated dipolar fields which are identical for all the Na sites. They were calculated assuming ordered moments of 1.89 μ_B, oriented along different axes, and for either ferromagnetic or antiferromagnetic interchain order. The obtained values are of the same order of magnitude as the experimental result, but they

TABLE I. Internal field H_{int} at the Na sites for different orientations of the V moments and for either ferromagnetic or antiferromagnetic interchain ordering. Ordered moments of 1.89 μ_B were assumed.

Direction of alignment of the moments	Interchain ordering	H_{int} (G) ± 2%
a axis	Ferromagnetic	1720
	Antiferromagnetic	570
b axis	Ferromagnetic	1550
	Antiferromagnetic	1050
c axis	Ferromagnetic	1720
	Antiferromagnetic	1720

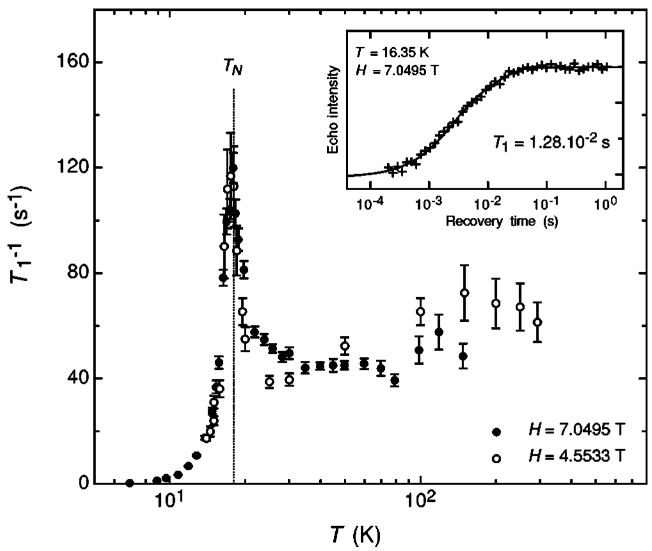

FIG. 13. ^{23}Na spin-lattice relaxation rate T_1^{-1} as a function of temperature T. The maximum of T_1^{-1} at the critical temperature is indicated by the dotted vertical line. The inset shows an example of the echo intensity as a function of the recovery time; the solid line is the best fit using the recovery function (26).

do not allow one to extract rigorous information about the orientation of the ordered moments, except that antiferromagnetic order along the a axis seems very unlikely. The uncertainity is, in particular, due to the fact that in the calculations we considered only dipolar coupling. In addition, the moments need not be aligned along the same direction, and their magnitude might also be reduced (as was suggested in the case of LiVGe$_2$O$_6$, see Ref. 9).

V. NMR SPIN-LATTICE RELAXATION RATE

In order to probe the low-energy spin excitations in NaVGe$_2$O$_6$ at low temperatures, we measured the spin-lattice relaxation rate $T_1^{-1}(T)$ by monitoring the recovery of the ^{23}Na nuclear magnetization after the application of a long comb of rf pulses, in the temperature range between 2 and 300 K. The experiments were performed by irradiating a frequency window of about 100 kHz. Above T_N, the irradiation frequency was chosen to be in the center of the central line, while below T_N we centered the window at approximatively the center of the broadened line. In both cases, a double recovery

$$m(t) = m_\infty[1 - D(0.6e^{-t/6T_1} + 0.4e^{-t/T_1})], \tag{26}$$

characteristic of $I=3/2$ nuclei,[24] with t the time variable and a constant $D \approx 1$, was observed.

In Fig. 13 we display the temperature dependence of the spin-lattice relaxation rate. A prominent peak in $T_1^{-1}(T)$ reflects the phase transition at $T_N=18$ K. Above T_N, T_1^{-1} varies only weakly with temperature and is not much affected by changing the field from 4.5533 to 7.0495 T. Those features are typical for a spin-lattice relaxation driven by the spin flips of the V^{3+} paramagnetic moments whose dynamics is characterized by a short correlation time τ, i.e., $\omega\tau \ll 1$. In this scenario[22]

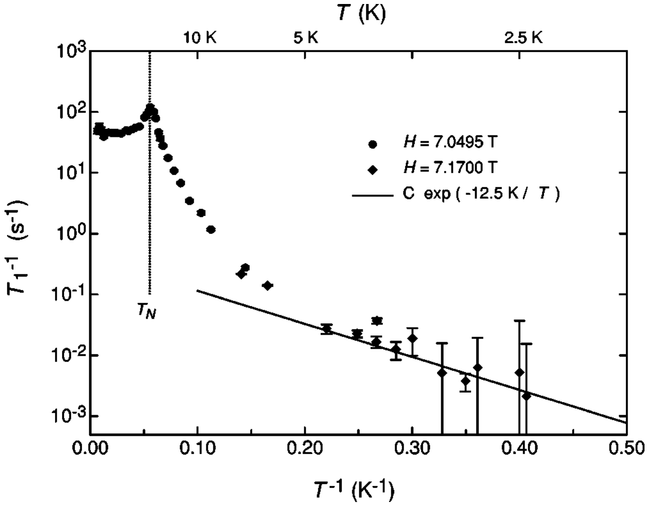

FIG. 14. ^{23}Na spin-lattice relaxation rate T_1^{-1} as a function of inverse temperature T^{-1}. The solid line represents the function $T_1^{-1}=C\ \exp(-\Delta/T)$ with $\Delta=12.5$ K.

$$T_1^{-1} \sim \frac{2}{5}\gamma^2 A^2 S(S+1)\tau, \tag{27}$$

where γ is the gyromagnetic ratio of the Na nuclei, A is the hyperfine coupling, and S is the spin of the magnetic moments. With $T_1^{-1}=50$ s^{-1}, $\gamma=7.0746\times10^7$ s^{-1} T^{-1} and $A \sim 0.1$ T, we estimate the correlation time of the V^{3+} moments to be $\tau\sim 1.25\times10^{-12}$ s.

Below T_N, T_1^{-1} decreases by orders of magnitude with decreasing temperature (a factor of 10^5 from 18 to 2.5 K, as shown in Fig. 14), indicating the formation of a gap in the spectrum of magnon excitations in the antiferromagnetically ordered state. This is supported by $T_1^{-1}(T)$ well below T_N, which varies according to

$$T_1^{-1}(T) \sim Ae^{-\Delta/T}, \tag{28}$$

as is emphasized by the solid line in Fig. 14. The magnon processes which lead to spin-lattice relaxation may be very complicated by involving several real and/or virtual magnons. At low temperatures, however, it is fair to assume that a two-magnon process, namely the scattering of a magnon at the nucleus with a nuclear spin-flip (Raman process), dominates.[25] In this case, $T_1^{-1}(T)$ is given by Eq. (28), and Δ corresponds to the gap in the magnon spectrum. Such a gap is usually attributed to an easy-axis single-ion magnetic anisotropy term in the Hamiltonian, of the form $D\Sigma_i\, S_{i,z}S_{i,z}$ with $D<0$.[26,27]

In our case, the uncertainty of the data at the lowest temperatures allows only for an estimate of the value of the gap Δ/k_B, of the order of 12 K. If a small amount of magnetic impurities, not indicated by the low-temperature susceptibility, were present, the actual value of the gap could be somewhat larger.

VI. NMR SPIN-SPIN RELAXATION RATE

Our measurements of the spin-spin relaxation rate T_2^{-1} as a function of temperature were made in the range between 2

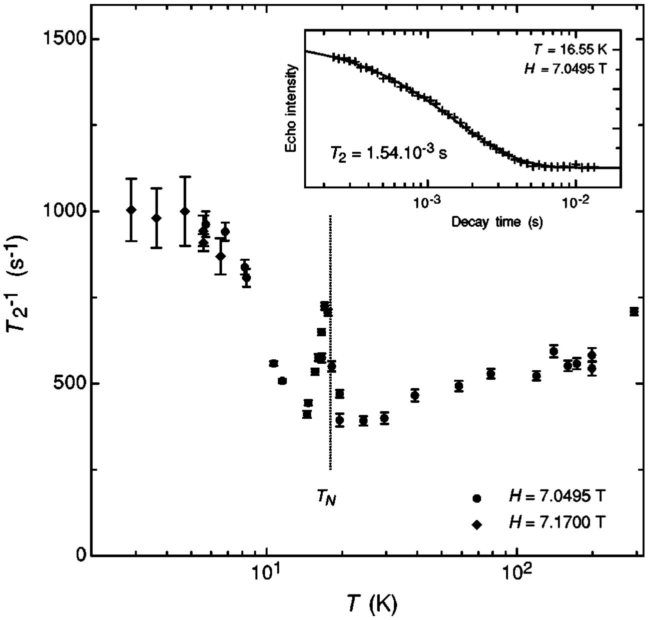

FIG. 15. ^{23}Na spin-spin relaxation rate T_2^{-1} as a function of temperature *T*. The inset shows an example of the echo intensity as a function of the decay time; the solid line is the best fit using the exponential decay function in Eq. (29).

and 300 K. The spin-echo lifetime T_2^* was obtained by monitoring the spin-echo intensity as a function of the pulse delay τ in the $\pi/2$-delay-π echo sequence. The irradiation conditions were chosen to be the same as in the T_1 experiments. At all temperatures, the intensity decayed according to

$$I(t) = I_0 e^{-\tilde{t}/T_2^*}. \qquad (29)$$

Here, $\tilde{t}=2(2/\pi\cdot t_{\pi/2}+d)+t_\pi\approx 2d$,[28] where $t_{\pi/2}$ and t_π are the durations of the pulses, and *d* is the delay between them. The spin-spin lattice relaxation rate was then calculated from

$$T_2^{-1} = T_2^{*-1} - T_1^{-1} \approx T_2^{*-1}. \qquad (30)$$

The last approximation is justified because $T_2^{*-1} \approx 10 \cdot T_1^{-1}$.

In Fig. 15 we display the temperature dependence of the spin-spin relaxation rate, measured for $H=7.0495$ T. A prominent peak in $T_2^{-1}(T)$ is observed at 17.5±0.5 K, and reflects the phase transition at T_N. Below that peak, $T_2^{-1}(T)$ exhibits an unexpected upturn with decreasing temperature and approaches a constant value at temperatures less than 5 K. Generally, T_2^{-1} is determined by the slow fluctuations of the internal magnetic field at the Na sites. Since in our case $T_2^{-1} \gg T_1^{-1}$, these fluctuations must basically be given by spin-spin interactions between the Na nuclei. In the antiferromagnetically ordered state, besides the direct dipolar interaction, also a magnon mediated interaction is expected to play a role. At any rate, it is not easy to see how this would lead to an increase of T_2^{-1} at lower temperatures and we have no reasonable explanation for this particular feature.

VII. COMPARISON WITH $LiVGe_2O_6$

From the structural point of view, $LiVGe_2O_6$ is very similar to $NaVGe_2O_6$. More precisely, the two substances share the same space group $P2_1/c$, and the lattice parameters differ by less than 1.5%. Moreover, both compounds contain chains of VO_6 octahedra, kept apart by GeO_4 tetrahedra.[7] Previously, we and other authors reported dc susceptibility and NMR studies on $LiVGe_2O_6$.[7–9] The results turned out to be qualitatively the same as those for $NaVGe_2O_6$ reported in this work. Below we focus our attention on the most evident quantitative differences.

TABLE II. Comparison of data extracted from dc susceptibility measurements on $LiVGe_2O_6$ and $NaVGe_2O_6$.

	$LiVGe_2O_6$	$NaVGe_2O_6$
T_{max}(K)	62	25
J/k_B(K)	47.0	18.9
T_N(K)	25	18
$J_\perp/k_B$(K)	3.4	3.4
$J_\perp/J$	0.07	0.18

The dc susceptibility of $LiVGe_2O_6$ $\chi(T)$ shows a maximum at $T_{max}=62$ K and a kink at $T_N=25$ K, from which the intra- and interchain couplings may be obtained in the manner described in Sec. III. The calculated values are shown in Table II. While the interchain coupling turns out to be approximatively the same, the intrachain coupling in $LiVGe_2O_6$ is about a factor of 3 larger than that in $NaVGe_2O_6$. This is somewhat surprising and indicates that even small differences in the orientations of the orbitals involved in the exhange interaction can affect the effective coupling between the moments at the V sites.

$LiVGe_2O_6$ has been the subject not only of NMR experiments, but also of neutron scattering[10] and muon spin resonance experiments.[29] It has been concluded that the low-temperature phase is antiferromagnetically ordered with a ferromagnetic interchain coupling; the magnitude of the ordered moments was reported to be $1.14\mu_B$, a much smaller value than expected from the *g*-factor inferred from the susceptibility. Using the above value for the ordered moment and single crystal NMR-experiments results, the authors of Ref. 9 suggested that the ordering occurs along the *c* axis. Our data are consistent with a similar scenario for $NaVGe_2O_6$.

VIII. CONCLUSIONS

$NaVGe_2O_6$ can be considered as a quasi-one-dimensional $S=1$ spin system only at temperatures much higher than the corresponding equivalent of the intrachain coupling $J/k_B \sim 19$ K. The expected Haldane phase, with a Haldane gap Δ_H/k_B of the order of 8 K, does not develop because the system orders antiferromagnetically below 18 K. The interchain coupling, $J_\perp/k_B \sim 3.4$ K, estimated from the $\chi(T)$ data, is by far sufficient to explain the suppression of the Haldane gap. The decay of the spin-lattice relaxation rate $T_1^{-1}(T) \sim \exp(-\Delta/k_BT)$ observed at $T \ll T_N$ indicates the opening of a gap $\Delta/k_B \leqslant 12$ K in the magnon excitation spectrum of the three-dimensional antiferromagnetically ordered system. This phenomenon is attributed to fluctuations of the two

3*d*-electrons orbitals of the V^{3+} ions, leading to an easy-axis single-ion anisotropy term in the Hamiltonian.

Further experiments with single crystals, aiming at obtaining more information on the orientation and the magnitude of the components of the electric field tensor, the internal field, and the eventual magnetic anisotropy seem to be in order.

ACKNOWLEDGMENTS

We are grateful to M. Sigrist and F. Alet for useful discussions. The numerical simulations were performed using the Asgard cluster at ETH Zürich. S.W. acknowledges support by the Swiss National Funds.

---

[1] F. D. M. Haldane, Phys. Lett. **93A**, 464 (1983).

[2] J. Renard, L. P. Regnault, and M. Verdaguer, J. Phys. (Paris) **49**, C8-1425 (1988).

[3] H. Mutka, C. Payen, P. Molinie, J. L. Soubeyroux, P. Colombet, and A. D. Taylor, Phys. Rev. Lett. **67**, 497 (1991); M. Takigawa, T. Asano, Y. Ajiro, and M. Mekata, Phys. Rev. B **52**, 13087 (1995).

[4] W. J. L. Buyers, R. M. Morra, R. L. Armstrong, M. J. Hogan, P. Gerlach, and K. Hirakawa, Phys. Rev. Lett. **56**, 371 (1986).

[5] G. Xu, J. F. DiTusa, T. Ito, K. Oka, H. Takagi, C. Broholm, and G. Aeppli, Phys. Rev. B **54**, R6827 (1996).

[6] J. Renard, M. Verdaguer, L. P. Regnault, W. A. C. Erkelens, J. Rossat-Mognot, and W. G. Stirling, Europhys. Lett. **3**, 945 (1987); A. Zheludev, S. E. Nagler, S. M. Shapiro, L. K. Chou, D. R. Talham, and M. W. Weisel, Phys. Rev. B **53**, 15004 (1996).

[7] P. Millet, F. Mila, F. C. Zhang, M. Mambrini, A. B. Van-Osten, V. A. Paschenko, A. Sulpice, and A. Stepanov, Phys. Rev. Lett. **83**, 4176 (1999).

[8] J. L. Gavilano, S. Mushkolaj, H. R. Ott, P. Millet, and F. Mila, Phys. Rev. Lett. **85**, 409 (2000).

[9] P. Vonlanthen, K. B. Tanaka, A. Goto, W. G. Clark, P. Millet, J. Y. Henry, J. L. Gavilano, H. R. Ott, F. Mila, C. Berthier, M. Horvatic, Y. Tokunaga, P. Kuhns, A. P. Reyes, and W. G. Moulton, Phys. Rev. B **65**, 214413 (2002).

[10] M. D. Lumsden, G. E. Granroth, D. Mandrus, S. E. Nagler, J. R. Thompson, J. P. Castellan, and B. D. Gaulin, Phys. Rev. B **62**, R9244 (2000).

[11] A. N. Vasiliev, T. N. Voloshok, O. L. Ignatchik, M. Isobe, and Y. Ueda, JETP Lett. **76**, 30 (2002).

[12] N. W. Ashcroft and N. D. Mermin, *Solid State Physics* (Saunders College Publishing, Orlando, 1976).

[13] The quantum Monte Carlo simulations were performed using a stochastic series expansion (Ref. 14) code based on the ALPS library (Ref. 15).

[14] A. W. Sandvik, Phys. Rev. B **59**, R14157 (1999); F. Alet, S. Wessel, and M. Troyer, cond-mat/0308495.

[15] M. Troyer *et al.*, Lect. Notes Comput. Sci. **1505**, 191 (1998). Source codes of the libraries are available from http://alps.compphys.org/

[16] A. Koga and N. Kawakami, Phys. Rev. B **61**, 6133 (2000).

[17] Y. J. Kim and R. J. Birgeneau, Phys. Rev. B **62**, 6378 (2000).

[18] D. J. Scalapino, Y. Imry, and P. Pincus, Phys. Rev. B **11**, 2042 (1975); H. J. Schulz, Phys. Rev. Lett. **77**, 2790 (1996).

[19] C. Yasuda *et al.*, cond-mat/0312392.

[20] A. Kawaguchi, A. Koga, K. Okunishi, and N. Kawakami, Phys. Rev. B **65**, 214405 (2002).

[21] G. C. Carter, L. H. Bennett, and D. J. Kahan, *Metallic Shifts in NMR* (Pergamon Press, Oxford, 1977) Part 1, Chap. 5.

[22] A. Abragam, *Principles of Magnetic Resonance* (Oxford Science Publications, Oxford, 1960).

[23] S. Yamamoto and S. Miyashita, Phys. Rev. B **48**, 9528 (1993).

[24] W. W. Simmons *et al.*, Phys. Rev. **127**, 1168 (1962).

[25] J. Barak, A. Gabai, and N. Kaplan, Phys. Rev. B **9**, 4914 (1974).

[26] V. Jaccarino, in *Magnetism IIA*, edited by G. T. Rado and H. Suhl (Academic Press, New York, 1965).

[27] D. Hone, V. Jaccarino, T. Ngwe, and P. Pincus, Phys. Rev. **186**, 291 (1969).

[28] C. P. Slichter, *Principles of Magnetic Resonance*, 3rd enlarged and updated ed. (Springer-Verlag, Berlin, 1990).

[29] S. J. Blundell, C. A. Steer, F. L. Pratt, I. M. Marshall, W. Hayes, and R. C. C. Ward, Phys. Rev. B **67**, 224411 (2003).